

A. Coupled Wave Theory

We provide the following introduction to Coupled Wave Theory (CWT) to explain the notion of open-closed channels and distributed feedback¹⁻³. Helmholtz's equation for the electric field, in a medium that consists of several layers along z , here Air-Membrane-Air, is given by:

$$\nabla^2 \mathbf{E}(\boldsymbol{\rho}, z) + k_0^2 \varepsilon_r(\boldsymbol{\rho}, z) \mathbf{E}(\boldsymbol{\rho}, z) = 0 \quad (1)$$

where $\boldsymbol{\rho}$ is the in-plane position vector. All layers can be considered to be periodic along x and y .

For all z , the permittivity verifies:

$$\varepsilon_r(\boldsymbol{\rho} + \mathbf{R}, z) = \varepsilon_r(\boldsymbol{\rho}, z) \quad (2)$$

where \mathbf{R} is the direct lattice vector. The permittivity can thus be expanded in Fourier series:

$$\varepsilon_r(\boldsymbol{\rho}, z) = \sum_{\mathbf{G}} \tilde{\varepsilon}_r(\mathbf{G}, z) e^{+j\mathbf{G}\cdot\boldsymbol{\rho}} \quad (3)$$

$$\tilde{\varepsilon}_r(\mathbf{G}, z) = \frac{1}{S} \iint \varepsilon_r(\boldsymbol{\rho}, z) e^{-j\mathbf{G}\cdot\boldsymbol{\rho}} d\boldsymbol{\rho} \quad (4)$$

where \mathbf{G} is the reciprocal lattice vector and S is the unit cell surface area. Besides, the electric field has to satisfy Bloch's theorem:

$$\mathbf{E}(\boldsymbol{\rho}, z) = e^{+j\mathbf{k}\cdot\boldsymbol{\rho}} \mathbf{E}_{\mathbf{kn}}(\boldsymbol{\rho}, z) \quad \text{with} \quad \mathbf{E}_{\mathbf{kn}}(\boldsymbol{\rho} + \mathbf{R}, z) = \mathbf{E}_{\mathbf{kn}}(\boldsymbol{\rho}, z) \quad (5)$$

Bloch fields are plane waves with a periodic envelope. Since these envelopes are periodic functions, they can also be expanded in Fourier series:

$$\mathbf{E}(\boldsymbol{\rho}, z) = e^{+j\mathbf{k}\cdot\boldsymbol{\rho}} \sum_{\mathbf{G}} \mathbf{E}_{\mathbf{kn}}(\mathbf{G}, z) e^{+j\mathbf{G}\cdot\boldsymbol{\rho}} \quad (6)$$

$$\mathbf{E}_{\mathbf{kn}}(\mathbf{G}, z) = \frac{1}{S} \iint \mathbf{E}_{\mathbf{kn}}(\boldsymbol{\rho}, z) e^{-j\mathbf{G}\cdot\boldsymbol{\rho}} d\boldsymbol{\rho} \quad (7)$$

We then obtain a system of Ordinary Differential Equations (ODE) that is valid in all layers, here air-membrane-air, along z :

$$\left(\frac{d^2}{dz^2} + k_0^2 \tilde{\varepsilon}_r(\mathbf{0}, z) - (\mathbf{k} + \mathbf{G})^2 \right) \mathbf{E}_{\mathbf{kn}}(\mathbf{G}, z) = -k_0^2 \sum_{\mathbf{G} \neq \mathbf{G}'} \tilde{\varepsilon}_r(\mathbf{G} - \mathbf{G}', z) \mathbf{E}_{\mathbf{kn}}(\mathbf{G}, z) \quad (8)$$

Eq. (8) has a structure similar to that of the equation describing Fano-Feshbach resonances². Fourier components $\mathbf{E}_{\mathbf{kn}}(\mathbf{G}, z)$ are called waves and this equation is thus referred to as a coupled-waves equation. In Eq. (8), waves are only coupled by the term on the right-hand side, *i.e.*, by the higher-order Fourier coefficients of the permittivity $\tilde{\varepsilon}_r(\mathbf{G} - \mathbf{G}', z)$.

In homogeneous layers, Eq. (8) reduces to:

$$\left(\frac{d^2}{dz^2} + k_0^2 \tilde{\varepsilon}_r(\mathbf{0}, z) - (\mathbf{k} + \mathbf{G})^2 \right) \mathbf{E}_{\mathbf{kn}}(\mathbf{G}, z) = 0 \quad (9)$$

Waves are thus only coupled in non-homogenous media. In homogeneous layers that extend to infinity, here air, waves are also referred to as decay channels and are classified into open and closed decay channels, depending on their asymptotic behavior:

$$k_0^2 \tilde{\epsilon}_r(\mathbf{0}, \pm\infty) - (\mathbf{k} + \mathbf{G})^2 > 0 \quad (\text{open or propagating}) \quad (10)$$

$$k_0^2 \tilde{\epsilon}_r(\mathbf{0}, \pm\infty) - (\mathbf{k} + \mathbf{G})^2 < 0 \quad (\text{closed or evanescent}) \quad (11)$$

For a sub-wavelength periodic membrane, there is only one open channel. All other channels are closed. In a typical scattering experiment, the incident and scattered waves are sent and received through the only open channel but the result of the experiment originates from the complex interferences amongst all coupled channels in the periodic membrane.

In our membrane, we consider a TM-like BIC mode around the Γ point of a square lattice. The periodic membrane analysed here is patterned in a square lattice with primitive lattice vectors a_1 and a_2 with corresponding reciprocal lattice vectors b_1 and b_2 (see Figure S1 below). To proceed, we make a few simplifying assumptions³. First, we consider perfect TM modes whose non-zero components are H_x, H_y, E_z , and neglect TM-TE coupling. Furthermore, we consider a solution that is separable in-plane and out-of-plane, *i.e.*, in \mathbf{G} and z . Lastly, we consider a distributed feedback mechanism that involves the waves in reciprocal lattice space around the Γ point. For example, as seen in Figure S1b, the red, blue and green arrows represent the equivalent waves to the $\Gamma^{(2)}, \Gamma^{(3)}$, and $\Gamma^{(4)}$ points respectively.

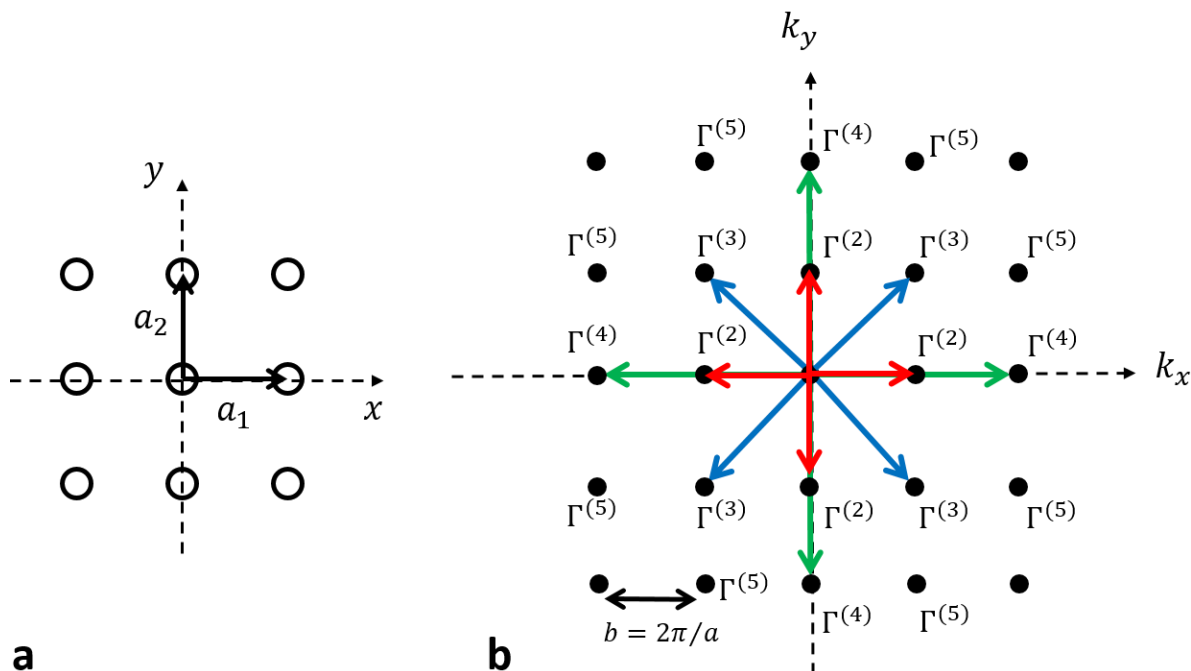


Figure S1 | **a**, In-plane geometry of a square lattice in real space with primitive translation vectors a_1 and a_2 . **b**, Reciprocal lattice space corresponding to the real space in (a). The red, blue and green arrows represent the equivalent waves to the $\Gamma^{(2)}, \Gamma^{(3)}$, and $\Gamma^{(4)}$ points respectively.

Taking all this into account, we obtain the following eigenvalue problem for the complex frequency³:

$$\frac{\omega_{kn}}{c} \mathbf{V} = [\mathbf{K} + \mathbf{C}_{1D} + \mathbf{C}_{rad} + \mathbf{C}_{2D}] \mathbf{V} \quad (12)$$

Here, ω_{kn} are the eigenvalues with complex eigen-frequencies and \mathbf{V} the eigen wave vectors of the reciprocal lattice. \mathbf{K} corresponds to the original uncoupled basic waves while coupling matrices \mathbf{C}_{1D} , \mathbf{C}_{rad} , and \mathbf{C}_{2D} correspond to 1D coupling between basic waves, radiative coupling, and 2D coupling via high-order waves respectively.

Here, we paint a more intuitive picture. If an initially guided wave of the homogeneous membrane turns into a leaky wave of the periodic membrane, a Fano-Feshbach resonance occurs⁴. Most of these Fano-Feshbach resonances have a finite lifetime but a precise engineering of the coupling amongst waves, *via* $\tilde{\epsilon}_r(\mathbf{G} - \mathbf{G}', z)$, can result in resonances whose lifetime tends towards infinity, *i.e.*, bound states in the continuum. Hence, BIC modes can be viewed as a superposition of waves whose respective radiation can be tuned to cancel each other, *i.e.*, total destructive interferences.^{1-3, 5}

B. Device fabrication

The BIC lasers are fabricated using standard nanofabrication techniques. We choose the active medium to be epitaxially grown multiple quantum wells of InGaAsP lattice-matched to InP substrate, tailored to emit in the telecom wavelength range. The gain material consists of nine $\text{In}_{x=0.564}\text{Ga}_{1-x}\text{As}_{y=0.933}\text{P}_{1-y}$ quantum well layers of 10nm thickness (bandgap wavelength of 1600nm) and $\text{In}_{x=0.737}\text{Ga}_{1-x}\text{As}_{y=0.569}\text{P}_{1-y}$ barrier layers of 20nm thickness (bandgap wavelength of 1300nm). An additional top barrier layer of 30nm makes the total height of the gain 300nm, which is covered by a protective 10nm thick InP capping layer. Fig. S2a shows the material stack without the InP cap layer. The InP cap is ultimately removed during fabrication. We spin coat ~100nm of PMMA and thermally deposit ~30nm of Chromium (Cr) on top of the bare wafer. Here, the Cr layer serves as a dry etch hard mask to attain and preserve the critical dimensions of the lasing membrane. While the PMMA layer serves as a sacrificial layer for the final and easy removal of the Cr (See Fig. S2b). We use electron beam lithography to define the device patterns on a hydrogen silsesquioxane (HSQ) negative tone resist coated wafer (See Fig. S2c). The spin-coating condition of HSQ is adjusted such that a 130 nm thick resist is spun on the wafer. After electron beam exposure and development of HSQ, the exposed HSQ serves as a mask for the subsequent reactive ion etching (RIE) process that defines the Cr hard mask. First, we dry etch the Cr using a combination of O₂ and Cl₂ plasma and subsequently we dry etch the PMMA layer with O₂ plasma (See Fig. S2d). Second, we dry etch the III-V material to define the cylindrical nanoresonators with the help of the Cr mask (See Fig. S2e). Note that this RIE, which uses a H₂:CH₄:Ar plasma, primarily etches the InGaAsP material but some InP material as well. Next, organic contaminations and polymer buildup during RIE are removed with a microwave oxygen plasma treatment, and the HSQ mask is removed with buffered oxide etch. Next, the Cr is removed simply by lifting off the PMMA layer in acetone solvent and slight sonication (See Fig. S2f). Subsequently, a substantial amount of InP substrate material is removed below InGaAsP MQW, with the help of photolithography and HCl solution⁶. Using photolithography, the areas to be wet-etched are opened in the negative-tone NR9 photoresist (Fig. S2g). Lastly, a diluted solution of hydrochloric

acid is used to selectively etch InP while minimally etching InGaAsP (Fig. S2h). The final structure can be seen in Fig. S2i as a schematic and in Fig. S3 as electron micrograph images. Note that, as a consequence of the resonator radius reduction during RIE and InP selective wet etching processes, radii of the resulting resonators are smaller than the radii after e-beam lithography. This reduction of radii is minimized with the use of the Cr metal mask.

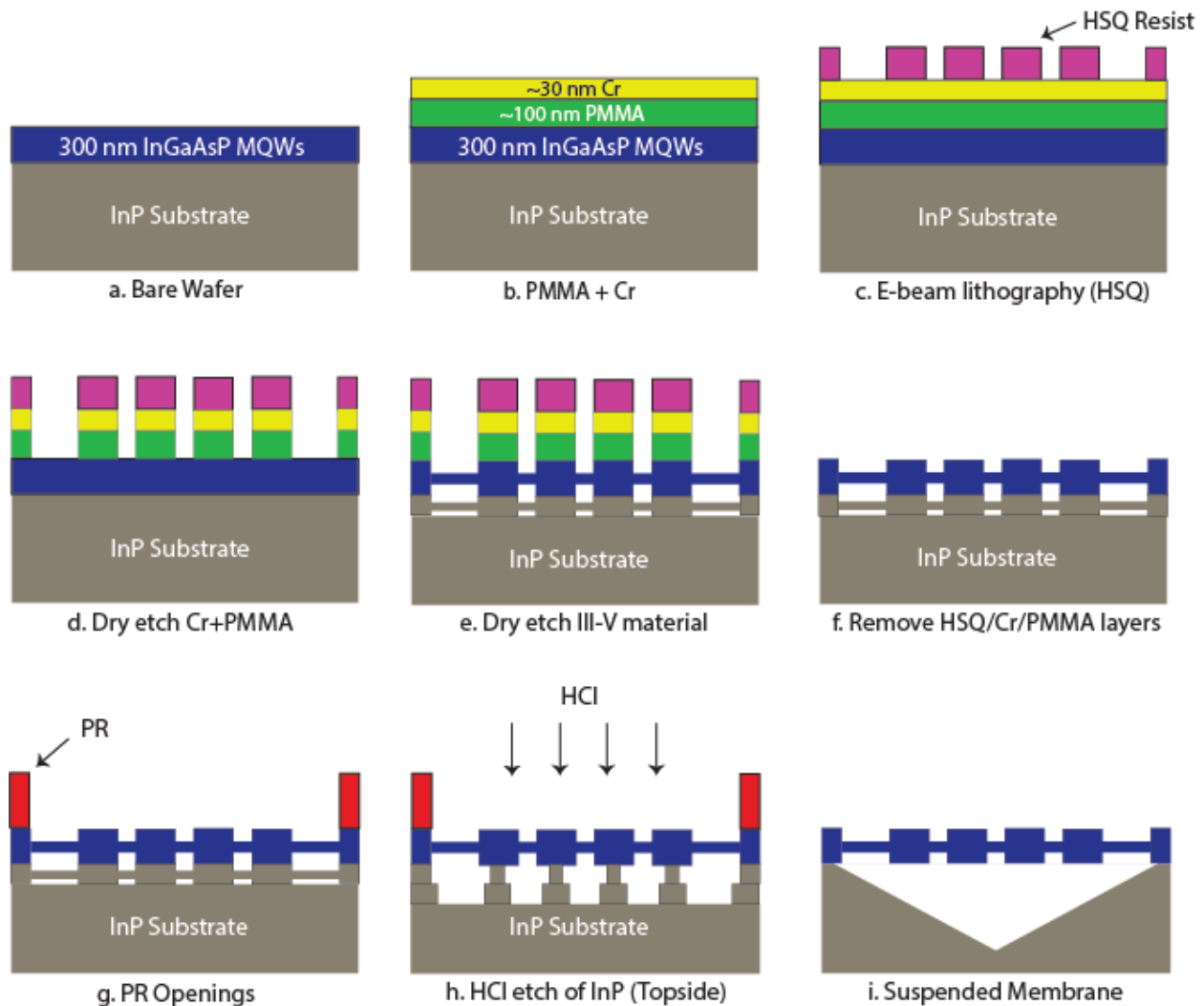


Figure S2 | a to i, Device fabrication process starting with the epitaxially grown multiple quantum wells on InP substrate and ending with the nanocylinders suspended membrane.

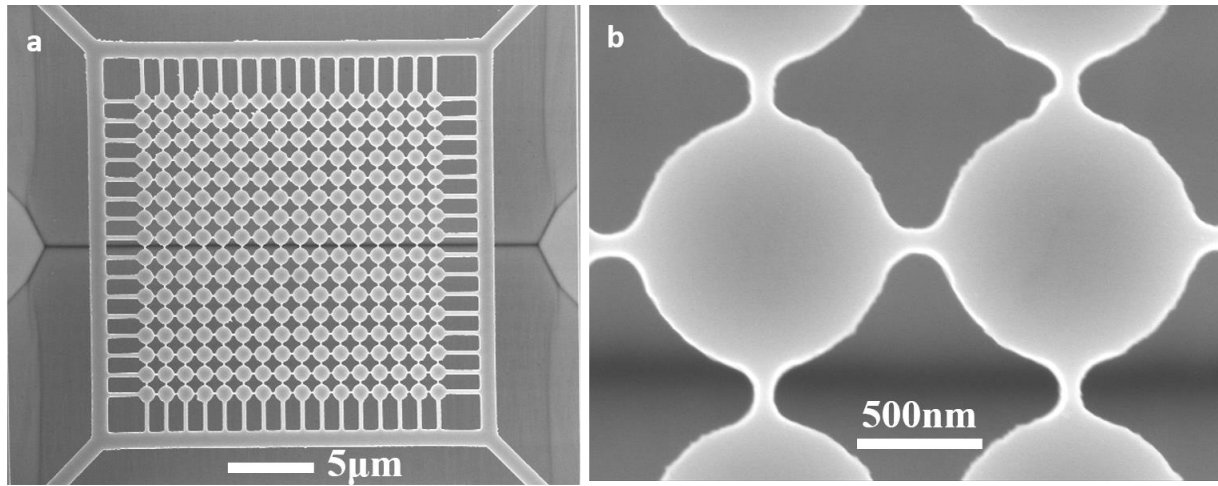


Figure S3 | **a**, Electron micrograph image of a fully suspended membrane structure with 16x16 cylindrical resonators interconnected by a network of bridges with a visible etch pit in the InP substrate and large openings for easy membrane release. **b**, Zoom-in image of two cylinders at the center of the array.

C. Odd and Even modes

We plot the complex dispersion relation for both odd and even modes (membrane mirror plane), in the wavelength range from 1.45 μm to 1.67 μm , in Fig. S4.

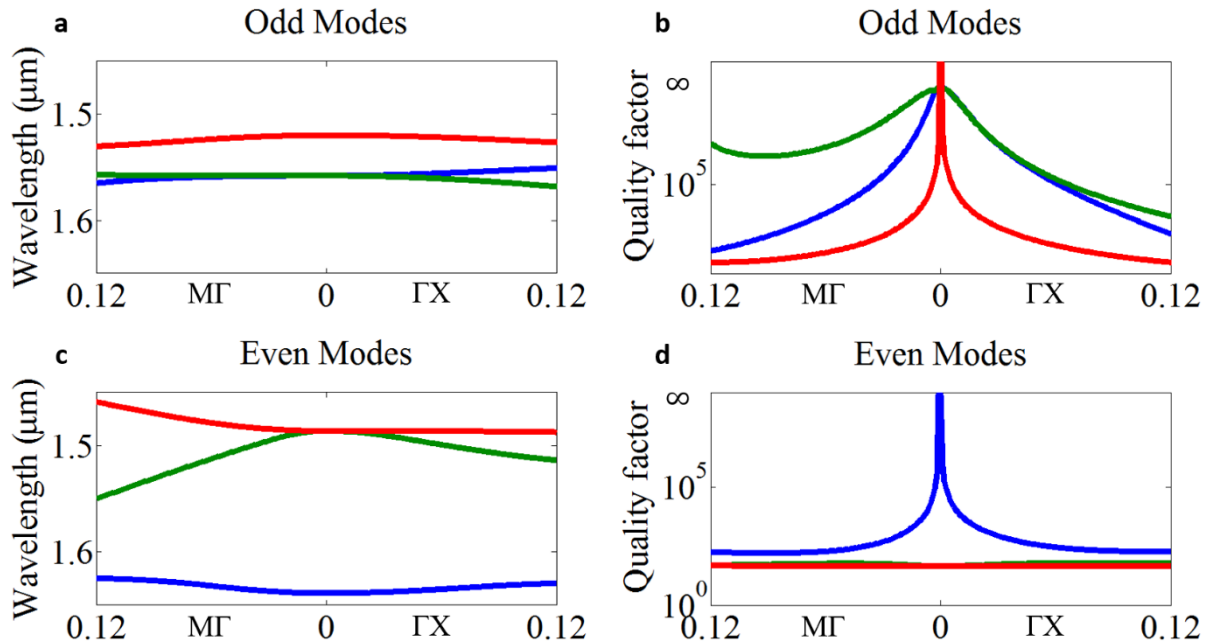


Figure S4 | Complex dispersion relation as function of k ($a/2\pi$) of the structure along $M\Gamma$ and ΓX in the wavelength range from 1.45 μm to 1.67 μm and for a BIC radius of 528.4 nm. Odd modes, **a**, Frequency vs. phase **b**, Quality factor vs. phase. Even modes, **c**, Frequency vs. phase **d**, Quality factor vs. phase.

As can be seen in Fig. S4, there are three odd modes and three even modes in this wavelength range. No mode has a higher overall quality factor than the two odd modes (doubly degenerate at Γ) around 1.55 μm , which are the BIC modes (Fig. S4b, blue and green lines). In addition, there are two symmetry-protected modes, one odd and one even, whose quality factors are high only at Γ (Fig. S4b, red and Fig. S4d, blue). Finally, there is a pair of even modes that are degenerate at Γ with a low quality factor (Fig. S4d, red and green).

D. Group Theory and tunable off- Γ BIC

The distinction between the ‘resonance-trapped’ and ‘symmetry-protected’ modes is further evident in the context of group theory⁷. In brief, spatial symmetries of a periodic membrane can be used to classify its modes. The point group of a square-lattice membrane suspended in air is the direct product of point groups C_{4v} and C_{1h} . Accordingly, its modes can be classified using the irreducible representations of both point groups. The two character tables below summarize how each irreducible representation behaves with respect to each symmetry operation.

C_{1h}	E	C_2
A	+1	+1
B	+1	-1

C_{4v}	E	$2C_4$	C_2	$2\sigma_v$	$2\sigma_d$
A_1	+1	+1	+1	+1	+1
A_2	+1	+1	+1	-1	-1
B_1	+1	-1	+1	+1	-1
B_2	+1	-1	+1	-1	+1
E	2	0	2	0	0

There are ten different modes that can exist in such a lattice (two times five). Since we restrict consideration to modes with an odd symmetry with respect to the membrane plane, only five are left: (B, A_1) , (B, A_2) , (B, B_1) , (B, B_2) , and (B, E) . At Γ , plane waves in free space admit an E representation and can thus only couple to (B, E) modes. Such modes have a low Q-factor on account of their radiative nature. In contrast, all other modes are uncoupled by virtue of symmetry, *i.e.*, they form symmetry-protected BICs, and thus have an infinite Q-factor. This was first reported by Paddon and Young⁸.

Furthermore, (B, A_1) , (B, A_2) , (B, B_1) , and (B, B_2) modes are all singly degenerate while the (B, E) mode is doubly degenerate. In our band diagram (Figure S4a), we see clearly one singly degenerate mode at 1520 nm and one doubly degenerate mode at 1558 nm. From the above symmetry considerations, we would thus expect only the lower wavelength mode to have an infinite Q-factor. However, we clearly see that this is not the case. This means that the doubly degenerate mode is not a BIC by virtue of symmetry-protection, *i.e.*, it must be a resonance-trapped BIC. Unlike previous works^{1, 9}, we show here that such BICs do not always happen away from high-symmetry points but can also occur at Γ . As such, our lasing structure fundamentally

differs from the work by Bo Zhen *et al.*¹⁰ where lasing originates from a symmetry-protected mode.

Moreover, the “resonance-trapped” BIC exploited in this work can be placed *by design* at either a high-symmetry point, such as the Γ -point, or at a generic point in k-space. In this work, we chose to exploit the BIC at Γ because many applications rely on surface emitting lasers. In this sense, compared to “symmetry-protected” BICs that have to operate at Γ , “resonance-trapped” BICs are more versatile. We show in Figure S5 below that the diverging quality factor associated with the “resonance-trapped” BIC modes (modes 1-2) can be placed off- Γ by choosing a membrane thickness of 290nm, *i.e.*, differing from the current 300nm used to fabricate all our BIC lasers. As seen in Figure S5a, modes 1-2 are the doubly degenerate BIC modes and mode 3 is the symmetry-protected mode. As seen in Figure S5b, for a thickness of 290nm, the diverging Q of the symmetry-protected mode remains at Γ whereas the diverging Q for modes 1-2 are now off- Γ . For the experiments, this membrane thickness is predefined during the finely controlled epitaxial growth.

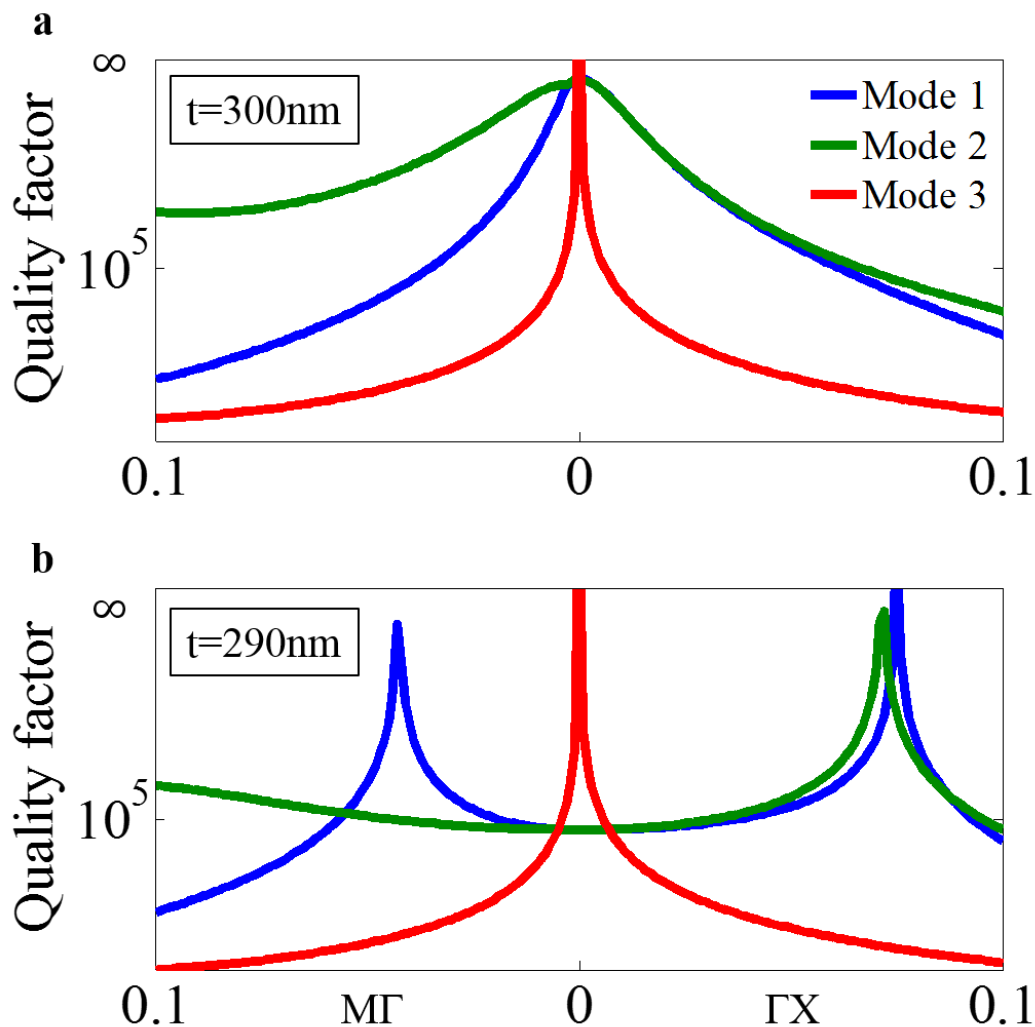


Figure S5 | **a**, Quality factor of modes 1-3 as a function of phase at optimal radius of 528.4nm and a membrane thickness of 300nm. **b**, Quality factor as a function of phase for a varied

membrane thickness of 290nm. Modes 1-2 are the doubly degenerate BIC modes and mode 3 is the symmetry-protected mode whose diverging Q remains at Γ whereas the diverging Q for modes 1-2 can be placed off- Γ .

E. CWT and BICs

We present below the eigen-frequencies acquired using CWT. When the quality factors diverge, it is a clear indication of destructive interference, *i.e.*, existence of a BIC: both symmetry-protected and resonance-trapped. The eigen-frequencies are compared with the results acquired from Finite Element Method (FEM) computation. We consider here the optimal BIC radius of 528.4nm with a membrane thickness 300nm (current experimental design) and a different thickness of 290nm (See Figures S6-S7).

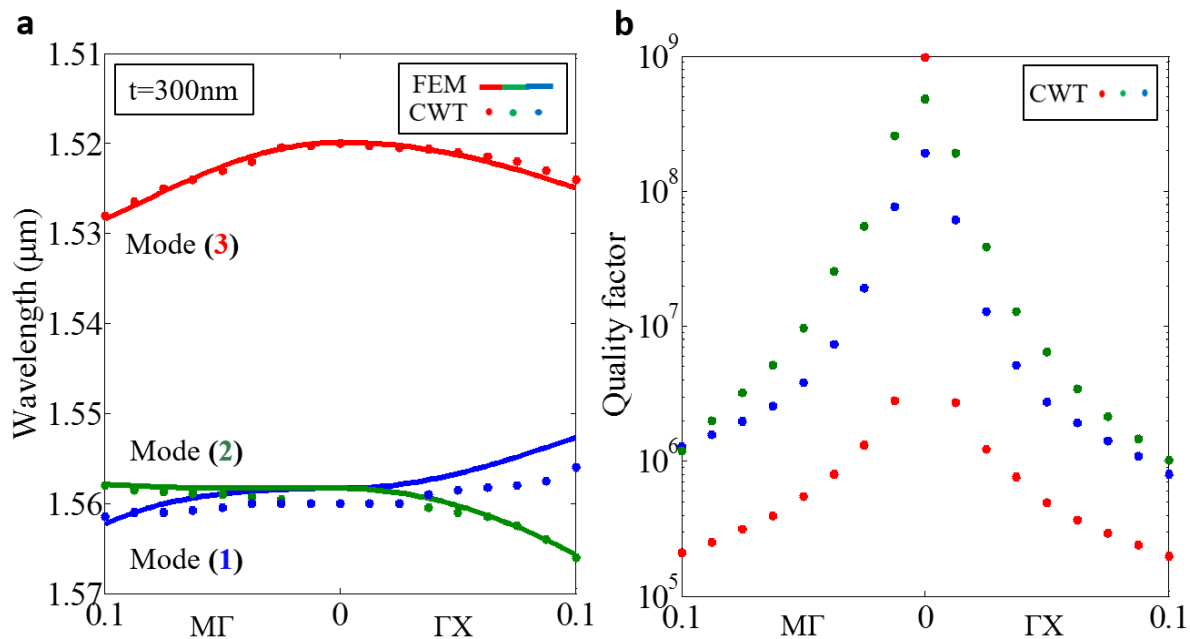


Figure S6 | Finite Element Method (FEM as solid lines) and Coupled-Wave Theory (CWT as dots) results with a membrane thickness of 300nm. **a**, Dispersion relation as function of k ($a/2\pi$) of the structure along $M\Gamma$ and ΓX for a BIC radius of 528.4 nm for resonance-trapped (Modes 1-2) and symmetry protected (Mode 3) modes. **b**, Quality factor as function of k ($a/2\pi$) for the three modes. The quality factor diverges for all three modes at Γ indicating a symmetry-protected BIC (Mode 3) and a degenerate resonance-trapped (Modes 1-2) BIC.

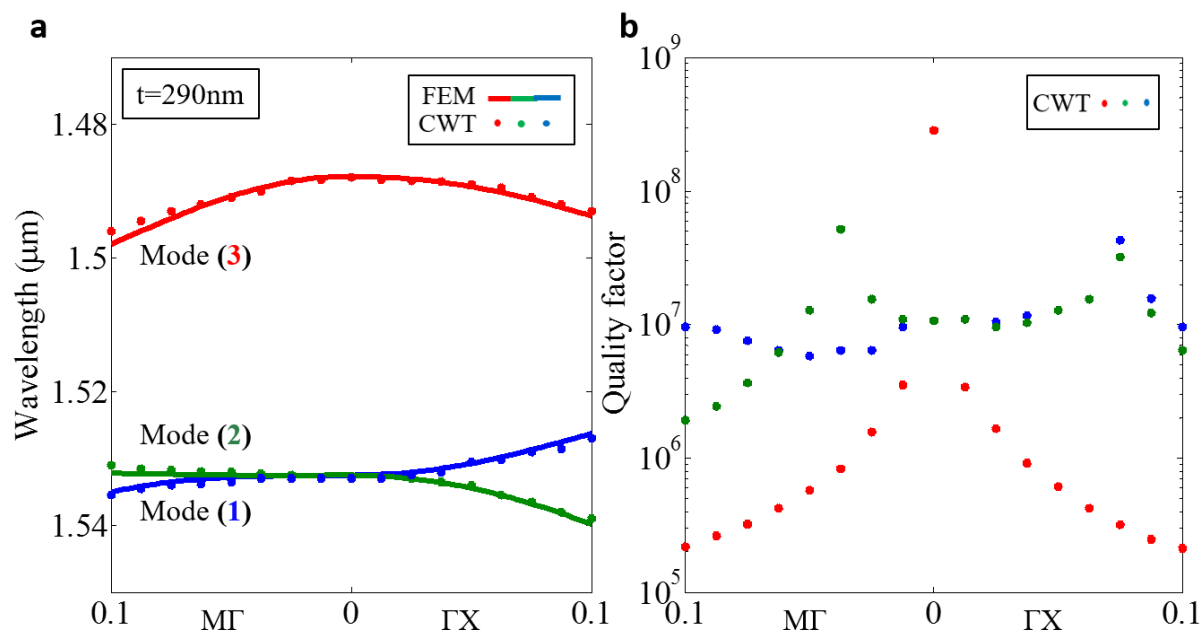


Figure S7 | Finite Element Method (FEM as solid lines) and Coupled-Wave Theory (CWT as dots) results with a membrane thickness of 290nm. **a**, Dispersion relation as function of k ($a/2\pi$) of the structure along $M\Gamma$ and ΓX for a BIC radius of 528.4 nm for resonance-trapped (Modes 1-2) and symmetry protected (Mode 3) modes. **b**, Quality factor as function of k ($a/2\pi$) for the three modes. The diverging quality factor corresponding to the symmetry-protected BIC (Mode 3) remains at Γ . However, for modes 1-2, the diverging quality factors occur away from the high symmetry point indicating multiple resonance-trapped BICs off- Γ .

In summary, resonance-trapped BICs are not restricted to high-symmetry points and the agreement between results from CWT and FEM support the destructive interference picture in the formation of resonance-trapped BICs.

F. Device characterization

To characterize the BIC lasers, we perform micro-photoluminescence measurement (schematically shown in Fig. S8) at room temperature. Devices under test are optically pumped by a 1064 nm laser with 12 ns pulse width, at a repetition rate of 300 kHz. A 20x long working distance microscope objective with a numerical aperture (NA) of 0.4 is used to focus the pump beam and simultaneously collect the emission from the sample. To minimize chromatic aberration, a telescope is introduced (lenses L-6 and L-7) to adjust the divergence of the pump beam such that the focal planes of the pump and emission wavelengths coincide. Using a double 4-f imaging system in conjunction with a pump filter, laser structures are either imaged onto an IR CCD camera (Indigo Alpha NIR), or spectroscopically measured with a monochromator (CVI Digikrom DK480) in conjunction with a cooled InGaAs detector in lock-in detection configuration. The monochromator can resolve a linewidth of ~ 0.33 nm.

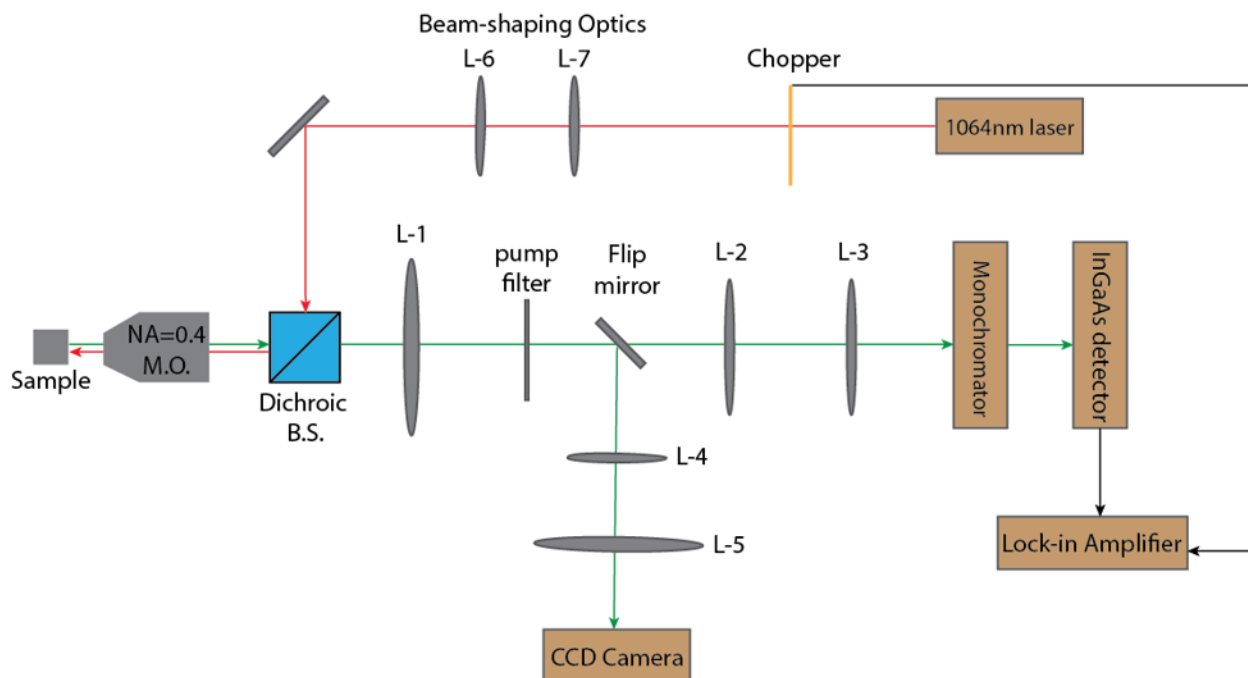


Figure S8 | Micro-photoluminescence setup used to measure laser emission from BIC lasers. Red color connection represents the pump path; green color connection represents the collection/imaging path; and black color connection represents electrical cables. The microscope objective (M.O.) with L-1,2,3 and L-1,4,5 compose a double 4-f imaging system for the CCD Camera and the monochromator, respectively.

G. Threshold Power Density versus Array Size

In our laser structures, the effect on the quality factor as a function of array size is easily discernible from the measured laser threshold powers. Here, we uniformly pump lasers of varying size and compare their threshold power densities (see Figure S9 below). For any given radius, the lasing threshold power density, P_{th} , decreases with increasing array size, N . This is clearly indicative of an increase in the quality factor as the laser array size increases. Furthermore, the material loss contribution to lasing threshold power is intrinsic to all lasers. Ideally, the material loss is the sole loss mechanism as the array size approaches infinity.

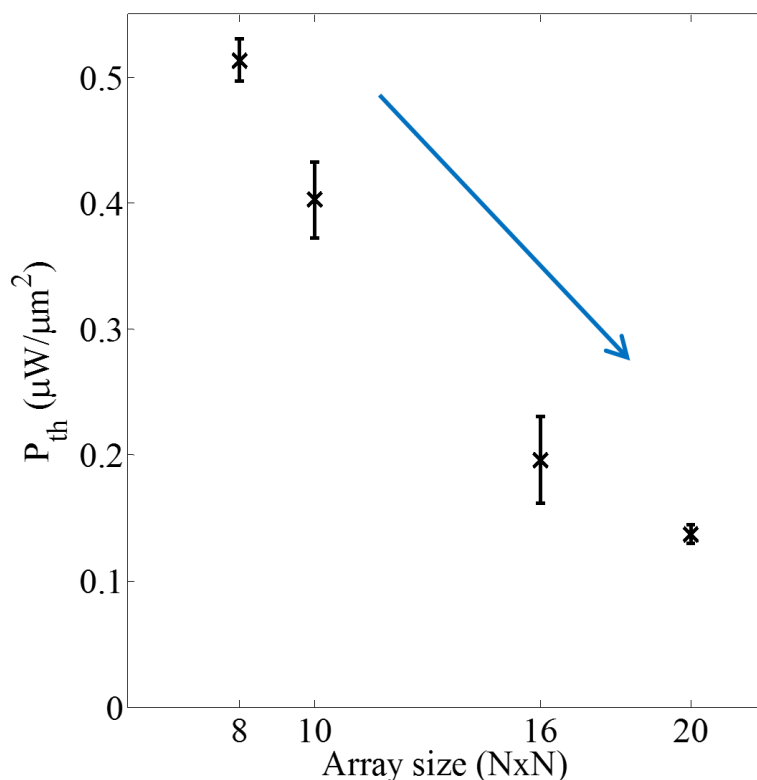


Figure S9 | Lasing threshold power densities, P_{th} ($\mu\text{W}/\mu\text{m}^2$), as a function of laser array size, N , for a given resonator radius ($R=530\text{nm}$). The effect on the quality factor due to the finiteness of the laser arrays is evident from the decreasing lasing thresholds with increasing size. As the array size increases, the cavity more closely resembles that of an infinite structure. This effect is observable irrespective of the resonator radius. The vertical error bars are the error in the threshold power over multiple measurements.

H. Far-field and Polarization Measurements

We show in Fig. S10 the calculated normalized far-field intensity profile for the lasing BIC mode with superimposed electric field¹¹. The IR CCD images of a suspended laser array in operation and its corresponding far-field emission can be seen in Fig. S11 and Fig. S12. The pump beam neatly overlaps the laser array (Fig. S11b) and the resulting emission collected over the camera bandwidth is presented in Fig. S11c. Far-field emission of the laser array operating above threshold is filtered around the lasing wavelength using a bandpass filter (FWHM of 40nm) as seen in Fig. S12. The emission profile is more prominent as the pump power is increased. The non-uniform pattern is partly a consequence of back reflections from the etched substrate below the laser array (*i.e.*, V-groove etch pit as seen in Fig S2i and S3a). Light emitted towards the bottom is reflected by the V-groove once or several times before passing through the suspended membrane. This leads to scattering in other directions and contributes to the experimentally observed far-field. Moreover, the finiteness of the array also leads to some in-plane emission.

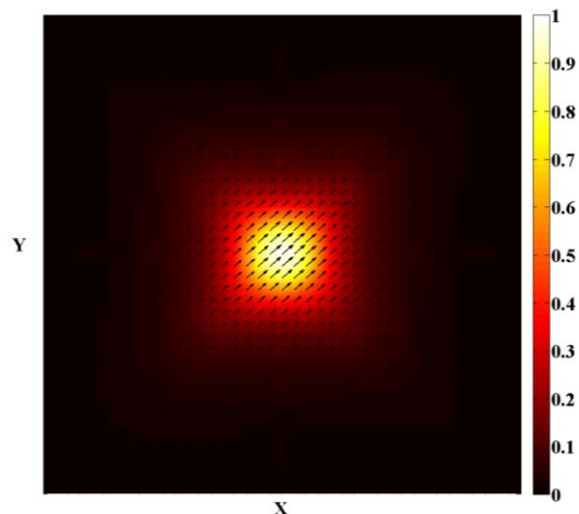


Figure S10 | Normalized far-field intensity profile for the lasing BIC mode with superimposed electric field.

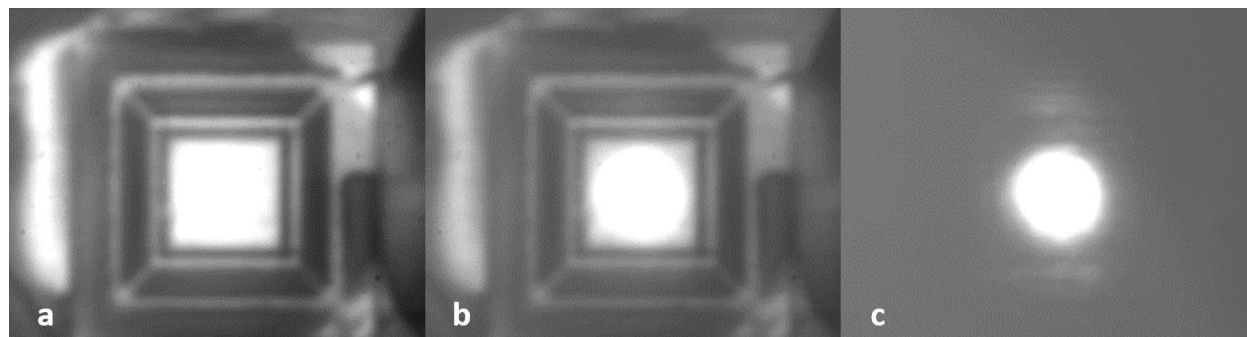


Figure S11 | **a**, IR CCD image of suspended laser array. **b**, Image of the array with overlapping pump beam. **c**, Image of emission from the laser array collected over the camera bandwidth.

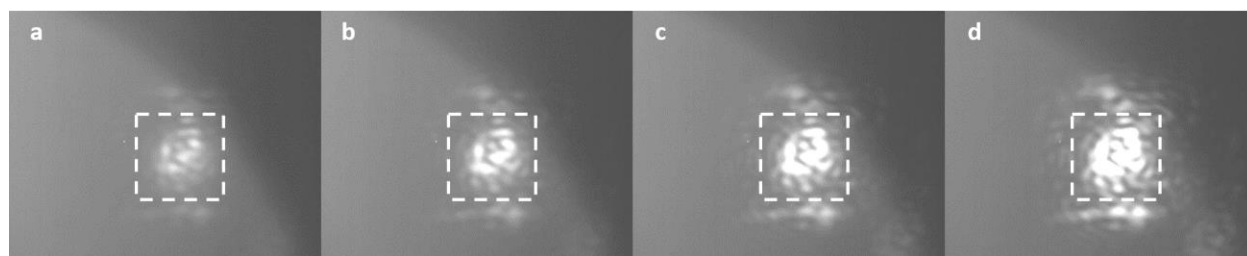


Figure S12 | Far-field emission of laser array over multiple pump powers with dotted outline indicating the physical size and location of the array. Emission profiles of lasers operating above threshold with increasing pump power: **a**, 82 μW **b**, 98 μW **c**, 111 μW **d**, 135 μW . Here, a bandpass filter with a FWHM of 40nm is utilized so as to only collect emission around the lasing wavelength and to avoid camera saturation.

As further identification of the lasing mode, we have conducted polarization measurements of our laser arrays operating above threshold (see Figure S13 below). There is agreement between the measured and calculated polarization ellipses as seen in Fig. S13b and c. There is observable

pinching in the measured ellipse corresponding to the predicted polarization ellipse. Note that the predicted ellipse does not account for the finiteness of the laser array. Furthermore, experimentally one of the degenerate modes wins mode competition and lases. Modes 1-2 are degenerate at Γ for infinitely large samples. Individually, the polarization ellipses for each of the two modes are orthogonal. Ideally, without imperfections, the two modes would be truly degenerate; thus the resulting polarization ellipse from the laser emission would be a circle.

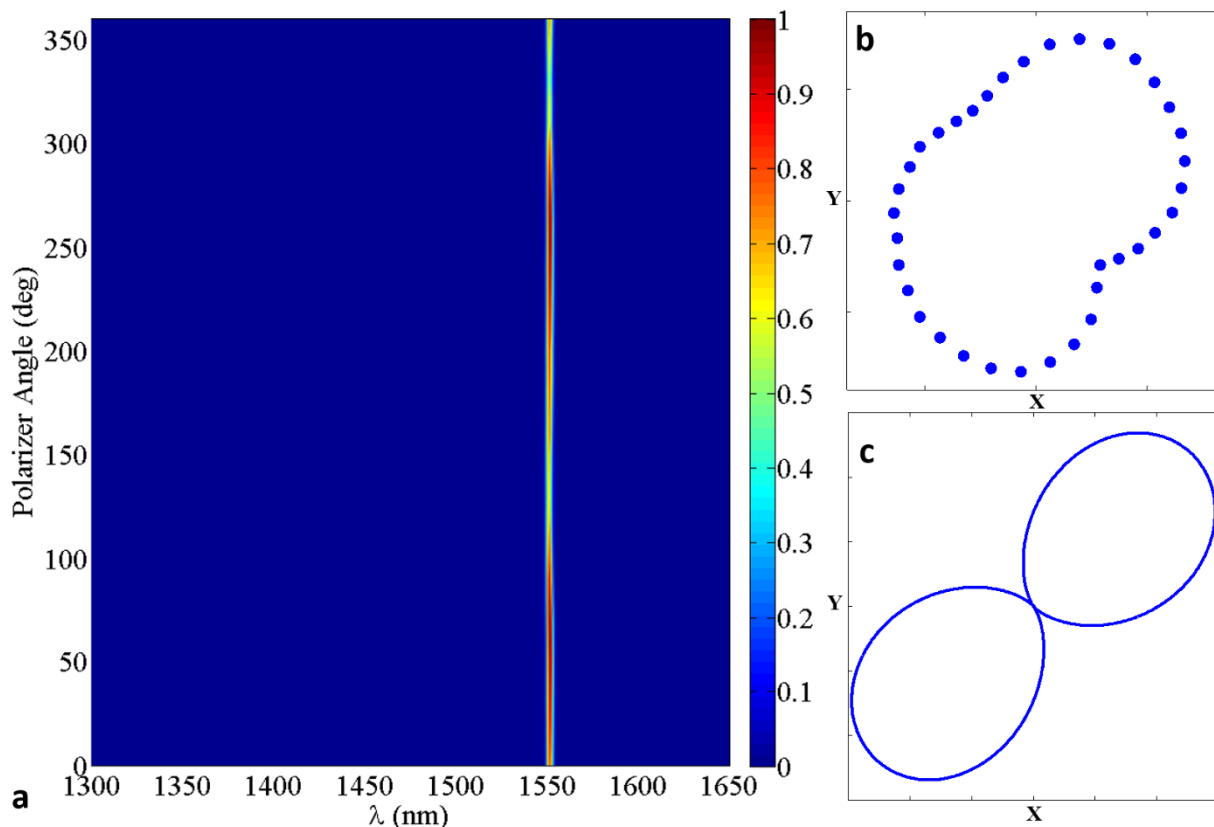


Figure S13 | Polarization measurement of laser operating above threshold. **a**, Photoluminescence spectra of a 16-by-16 laser array with a nanoresonator radius of 525 nm as a function of the polarizer angle. **b**, Measured polarization ellipse and **c**, predicted polarization ellipse not accounting for the finiteness of the lasing array. There is observable pinching in the measured ellipse corresponding to the ideal polarization ellipse.

References

1. C. Peng, Y. Liang, K. Sakai, S. Iwahashi, and S. Noda, "Three-dimensional coupled-wave theory analysis of a centered-rectangular lattice photonic crystal laser with a transverse-electric-like mode," *Phys. Rev. B* **86**, 035108 (2012).
2. Y. Yang, C. Peng, Y. Liang, Z. Li, and S. Noda, "Analytical Perspective for Bound States in the Continuum in Photonic Crystal Slabs," *Phys. Rev. Lett.* **113**, 037401 (2014).

3. Y. Yang, C. Peng, Y. Liang, Z. Li, and S. Noda, "Three-dimensional coupled-wave theory for the guided mode resonance in photonic crystal slabs: TM-like polarization," *Opt. Lett.* **39**, 4498 (2014).
4. H. Friedrich and D. Wintgen, "Interfering resonances and bound states in the continuum", *Phys. Rev. A* **32**, 3231 (1985).
5. C. W. Hsu, B. Zhen, A. D. Stone, J. D. Joannopoulos, and M. Soljacic, "Bound states in the continuum," *Nat. Rev. Mater.* **1**, 16048 (2016).
6. K. Srinivasan, P. E. Barclay, and O. Painter, "Fabrication of high-quality-factor photonic crystal microcavities in InAsP/InGaAsP membranes," *J. Vac. Sci. Technol. B* **22**, 875 (2004).
7. K. Sakoda, 'Optical Properties of Photonic Crystals,' 2nd Edition, Springer (2005).
8. P. Paddon and J. F. Young, "Two-dimensional vector-coupled-mode theory for textured planar waveguides," *Phys. Rev. B* **61**, 2090 (2000).
9. C. W. Hsu, B. Zhen, J. Lee, S-L. Chua, S. G. Johnson, J. D. Joannopoulos, and Marin Soljacic, "Observation of trapped light within the radiation continuum," *Nature* **499**, 188-191 (2013).
10. B. Zhen, S-L. Chua, J. Lee, A. W. Rodriguez, X. Liang, S. G. Johnson, J. D. Joannopoulos, M. Soljacic, and O. Shapira, "Enabling enhanced emission and low-threshold lasing of organic molecules using special Fano resonances of macroscopic photonic crystals," *Proc. Natl. Acad. Sci.* **110**, 13711-13716 (2013).
11. C. A. Balanis, 'Antenna Theory: Analysis and Design,' 3rd Edition, Wiley (2005).